Characterization of Polarized SAR Scattering of Breaking Waves Caused by Internal Solitary Waves

Hao Zhang, *Student Member, IEEE*, Junmin Meng, *Member, IEEE*, Lina Sun, Shibao Li, and Xinmiao Zhang

***Abstract*—Internal solitary waves (ISWs) resonate with meter-scale surface waves, which causes crests to overturn and waves to break strongly, generating many whitecaps. We analyze the polarized SAR characteristics of ISWs based on nonpolarized scattering theory and polarization decomposition theory. The surface breaking waves induced by ISWs generate short-scale waves carrying Bragg waves on the one hand, which enhances the polarized Bragg scattering (PD) contribution at the decimeter or centimeter scale and generate additional nonpolarized scattering (NP) contribution through specular scattering on the other hand. The copolarized scattering intensity in ISW regions is always higher than that in unperturbed sea surface under both L and C bands, with higher PD and NP contributions. The average PD is 1.3 (1.7) times higher than that of the unperturbed sea surface, and the average NP is approximately 82% (165%) higher than that of the sea surface. The PD and NP values associated with the convergent zones are always larger than those associated with the divergent zones, indicating that breaking waves mainly occur in convergence. The results of $H A \alpha$ decomposition show that the scattering mechanism of ISWs is surface scattering with reduced scattering entropy and mean scattering angle. We construct compact polarization based on fully polarized SAR, and extract polarization parameters that indicate increased degree of polarization at ISWs, which supports our inference of enhanced specular scattering.**

***Index Terms*—Breaking waves, internal solitary waves, nonpolarized scattering, polarimetric SaR.**

I. Introduction

SUBMESOSCALE dynamical processes known as oceanic internal waves are common in the ocean and propagate along the pycnocline with frequencies between inertial and Brunt–Väisälä frequencies, usually generated by tidal interactions with topography [1]. Internal waves, in most cases, can gradually become highly nonlinear, steepen and decompose into solitary wave packets consisting of several internal solitons, known as internal solitary waves (ISWs), which are characterized by strong nonlinearity, large amplitude, short period, and high speed [2], [3]. ISWs play an important role in biological primary production and the evolution of the climatic environment, with considerable implications for global marine ecosystems and ocean engineering. Especially near the continental shelf, nutrients in deep seawater can be transported to the surface layer, fostering the growth of coral reefs [4], [5], fish and other creatures [6], [7], [8]; ISWs also harm to submarines [9], drilling platforms [10], and oil pipelines [11].

In the past few decades, remote sensing has become the most common means for investigating ISWs [12]. Synthetic Aperture Radar (SAR) is an active microwave sensor with high resolution, full polarization, and all-weather observation capabilities compared to optical remote sensing [13]. SAR uses microwaves with centimeter or decimeter-scale wavelengths to sense (typical wavelengths for L- and C- band are 15 cm and 6 cm). SAR sense sea roughness on a scale comparable to the electromagnetic waves they emit. In general, the SAR-measured backscatter energy depends on the sea surface roughness, which is modulated by the capillary generated by the local wind and small gravity waves (centimeter-scale resonant Bragg waves). Resonant Bragg waves are modulated by long waves through tilted hydrodynamic effects, as well as by surface winds and other oceanic processes, allowing SAR to make 2-D observations of the sea surface roughness when it is modified by the interaction of internal waves with near-surface currents and wind [14].

ISWs will cause the convergence and divergence of water particles on the sea surface throughout their propagation, forming a spatial-temporally varying surface currents field. The varying currents field interact with the surface wind waves, modulating the Bragg waves, which are eventually detected by SAR [10]. The convergence region scatters more electromagnetic waves back to the sensor, and the energy received by the sensor is stronger. Therefore, in the SAR image, ISWs often appears as bright (convergence, rough) and dark (divergence, smooth) stripes [14]. Based on images captured by various SAR sensors, there are numerous reports on ISWs, such as generation sources, hydrodynamic parameter inversion, deep learning applications, and radar scattering characteristics [15], [16], [17], [18], [19], [20], [21], [22], [23], [24]. However, a full quantitative analysis of SAR backscattering properties of ISWs, particularly the scattering characteristics of different bands, varied polarization, and different observation conditions, is urgently required. This difference in scattering capability is the basis of SAR imaging of ISWs.

Manuscript received 22 May 2023; revised 7 September 2023 and 30 October 2023; accepted 18 December 2023. Date of publication 20 December 2023; date of current version 16 January 2024. This work was supported in part by the National Natural Science Foundation of China under Grant U2006207 and Grant 42006164. *(Corresponding author: Junmin Meng.)*

Hao Zhang and Shibao Li are with the College of Oceanography and Space Informatics, China University of Petroleum, Qingdao 266580, China, and also with the First Institute of Oceanography, Ministry of Natural Resources, Qingdao 266061, China (e-mail: zhanghao@fio.org.cn; lishibao@upc.edu.cn).

Junmin Meng, Lina Sun, and Xinmiao Zhang are with the First Institute of Oceanography, Ministry of Natural Resources, Qingdao 266061, China (e-mail: mengjm@fio.org.cn; sunln@fio.org.cn; zhangxinmiao@fio.org.cn).

Digital Object Identifier 10.1109/JSTARS.2023.3345033

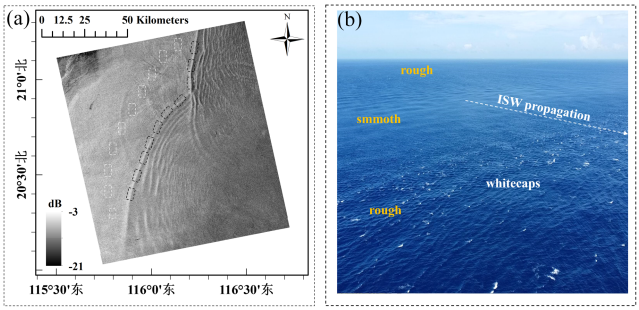

Fig. 1. (a) HH ENVISAT ASAR image in dB, South China Sea, April 20, 2008, the incident angle is 22.25°. (b) A photograph of a sea surface that has been ISWs modified; the white aligned dots are whitecaps from breaking waves.

In addition to capillary gravity waves, the ocean surface typically contains longer scale waves, in which winds continue to input energy, due to wave-wave interactions, thereby transferring energy from short waves to long waves, which finally break and produce whitecaps on the ocean surface. These breaking waves are important in momentum, energy, and gas exchange at the air–sea interface and effect the maximum height of surface waves [25]. Obviously, surface waves can also break in the absence of wind, such as when a swell on the shore.

Breaking waves may result from several formation mechanisms, such as those related to microbreaking of decimeter-scale waves and the formation of nonlinear structures, or those related to strong breaking of meter-scale waves and crests overturning. Resonance occurs for an ISW when its phase velocity matches the group velocity of the surface waves ($C^{sw}_{\text{group}} = C^{IW}_{\text{phase}}$) [26].

Due to the accumulation of energy, the crest will be violently overturned and broken even at modest wind. Based on the dispersion relation of deepwater waves, the wavelength of resonant surface waves is: $\lambda^{sw}_{\text{resonent}} = (8\pi/g)(C^{IW}_{\text{phase}})^2$. The phase velocities of ISWs are typically between 1.0 and 2.0 m/s, and the wavelengths of resonant surface waves range from 3 to 10 m. Therefore, both field observations and remote sensing images revealed an abundance of whitecaps caused by the breaking of meter-scale waves in the sea surface, where ISW pass, particularly in the convergence zone [27] [see Fig. 1(b)].

The contribution of ISW-induced wave breaking to SAR echoes is not entirely understood, and there are relatively few studies on this topic. Alpers described the SAR imaging process of ISW according to weak hydrodynamics and the Bragg scattering theory [14], but it ignored the scattering contribution of breaking waves and is unable to explain the spike-like pulse signal in SAR images. These breaking waves may scatter in a variety of ways, including edge diffraction from sharply crested waves, the quasi-specular backscattering from the steep forward faces of breaking waves, and the enhanced Bragg scattering due to small-scale roughness caused by wave breaking. Research hotspots in ISW SAR imaging include the question of whether breaking waves in the divergent and convergent zones differ significantly from one another and whether this difference is influenced by band and other environmental conditions.

According to Kudryavtsev et al., the scattering process associated with breaking waves can be described as nonpolarized (NP) backscattering, which is less sensitive to polarization and contributes significantly to HH and VV measurements [28]. The literature has noted that when ISWs cause surface waves to break at intermediate incidence angles, nonpolarized backscattering, which combined with polarized Bragg scattering constitutes copolarized sea surface backscattering [29], [30]. Thus, using polarimetric SAR, the observed radar scatter from sea surface may be decomposed into NP contributions from breaking waves and purely polarized Bragg scattering contributions. In addition, the polarization decomposition can be performed using four polarization channels to analyze the scattering characteristics of ISWs. It should be noted that the polarization in SAR electromagnetic waves represents the scattering randomness, and the higher the random scattering, the weaker the polarization; while the nonpolarization in wave breaking represents that its scattering characteristics are independent of polarization, and these two should not be confused.

This work is based on polarimetric SAR images to examine the polarimetric scattering properties of ISWs, including NP contributions associated with breaking waves, and the quantitative scattering differences in the convergent and divergent zones. The fully polarized SAR images with different bands (C, L) are considered to investigate the scattering characteristics in different detection conditions. Several polarized feature parameters are screened using polarization decomposition to further characterize the scattering features related to breaking waves caused by ISWs.

The rest chapters of this article are organized as follows: data and methodology are introduced in Section II, followed by an analysis of the polarization scattering properties of ISWs in Section III, a discussion of polarization decomposition in Section IV, and a conclusion in the final chapter Section V.

II. Data and Methods

A. SAR Images

ESA ENVISAT ASAR dual copolarization images and Japan ALOS PALSAR full polarization images are used. The C-band Advanced Synthetic Aperture Radar (ASAR) aboard ENVISAT, which was launched on March 1st, 2002, has five operational modes, including alternating polarization mode (AP). The L1-level Alternating Polarization Precision Image (APP) used in this work has an incidence angle between 21° and 34° and a spatial resolution of approximately 12.5 m × 12.5 m (range × azimuth). The PALSAR image resolution ranges from 24 to 89 m and the swath is between 20 and 65 km, providing SLC data of HH, HV, VH, and VV. The resolution of PALSAR images in this article is 9 m × 21 m (range × azimuth), and the incident angle is between 23° and 26°. Appendix A lists specific information of images.

The 10 m wind corresponding to the SAR image is matched using the fifth generation ECMWF reanalysis data collection (ERA5) [31], [32]. EAR5 provides hourly estimates of the atmosphere and ocean waves, where the spatial resolution of the 10 m high wind field is 0.25° × 0.25°. Appendix A lists the wind conditions of the SAR images, with most of them being at low wind, with wind speeds between 2 and 8 m/s.

Fig. 1 displays s a HH polarized ENVISAT ASAR image of an ISW packet propagating to the northwestward near Dongsha Island in the South China Sea on April 20, 2008. The sea surface features of ISWs in the figure are clear, and the stripes are first bright and then dark along the propagation direction, suggesting that it is a descending wave. The black and white boxes represent the region of interest of ISWs, and the sea background region is not disturbed by ISWs, respectively.

B. Nonolarized Scattering Theory

With regard to breaking waves, Kudryavtsev et al. proposed the nonpolarized scattering theory [28], [29], which expresses the copolarized scattering as the sum of the polarized two-scale Bragg scattering contribution and the nonpolarized scattering contribution (NP) associated with the breaking waves. The former is expressed as $\sigma_{qq}^{0,B}$, the latter is expressed as $\sigma^{0,wb}$. The NP scattering include the specular reflection in the forward faces of breaking waves and the incoherent backscattering produced by the small-scale surface roughness perturbation caused by breaking waves [33]. In the latter case, the waves breaking caused by ISWs may produce specular reflection in the wave front, therefore cannot be excluded according to the incident angle.

In nonpolarized scattering theory

$$\sigma_{qq}^{0} = \sigma_{qq}^{0,B} + \sigma^{0,wb} \tag{1}$$

where q represents horizontal (H) or vertical (V) polarization. The first term on the right ($\sigma_{qq}^{0,B}$) is polarization dependent, and the second term ($\sigma^{0,wb}$) is polarization independent. According to (1), the NP contribution is obtained using the copolarized scattering polarization difference (PD) and the Bragg scattering polarization ratio (PR)

$$\sigma^{0,wb} = \sigma_{VV}^{0} - \frac{\sigma_{VV}^{0} - \sigma_{HH}^{0}}{1 - \frac{\sigma_{HH}^{0,B}}{\sigma_{VV}^{0,B}}} = \sigma_{VV}^{0} - \frac{PD}{1 - PR}. \tag{2}$$

The PD is controlled by the surface roughness produced by wave components close to the Bragg wave number, therefore PD can maximize the polarized Bragg scattering contribution. The PR is determined by the local geometry and tilting effects [29]:

$$PR = \frac{\sigma_{HH}^{0,B}}{\sigma_{VV}^{0,B}} \approx \frac{|G_{HH}|^2}{|G_{VV}|^2}\left[1 + (g_{HH} - g_{VV})\, s_i^2\right] \tag{3}$$

where g_{qq} depends on the Bragg scattering coefficient G_{qq} and the incident angle θ, defined as

$$g_{qq} = 0.5 \frac{1}{|G_{qq}(\theta)|} \frac{\partial^2 |G_{qq}(\theta)|}{\partial \theta^2}. \tag{4}$$

In (3), $s_i^2 = s^2/2$ is the mean square slope in the direction of the incidence plane and s^2 is the mean square slope [22]

$$s^2 = 4.5 \times 10^{-3} \mathrm{In}\left(\eta^{-2} \mathrm{k_d} \frac{\mathrm{U_{10}^2}}{\mathrm{g}}\right) \tag{5}$$

where g is the gravity acceleration, U_{10} is the wind speed at 10 m, $k_d = k_B/4$ is the splitting wavenumber in the two-scale model, k_B is the Bragg wave number, $\eta = U_{10}\sqrt{\frac{k_p}{g}}$ is the inverse wave age, and k_p is the spectral peak wave number [29].

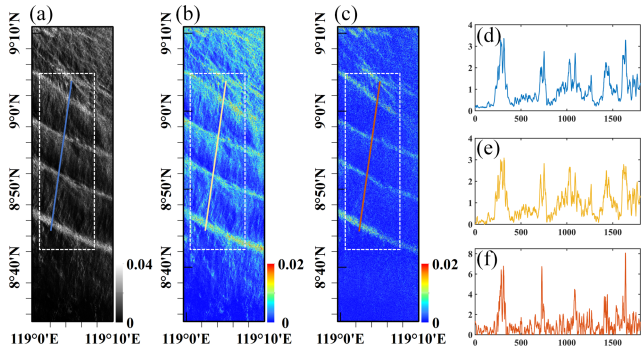

Fig. 2. ALOS PALSAR image acquired on May 19, 2010, the incidence angle is 25.72°. (a) VV (linear units). (b) PD represents the polarized Bragg scattering. (c) NP, the nonpolarized scattering. The colored solid lines in (a), (b), (c) are ISW profiles to be extracted, and the white dashed boxes represent the background region. The line graphs (d), (e), (f) depict the modulation index along the profile of interest in the images (a), (b), (c), which is normalized by the background region.

Polarimetric SAR images and the U_{10} are obtained, then the original dual copolarized image (HH/VV) can be converted into new images such as PR, PD, NP defined by (1)–(5). These images contain two types of radar scattering that are noticeably different from one another: polarized Bragg scattering (PD) provided by fast response short-scale waves and NP scattering provided by breaking waves.

III. Polarization Scattering Characteristics Analysis

Fig. 2 illustrates the multipolarized backscattering characteristics of ISWs in the ALOS PALSAR image, including σ_{HH}^{0}, PD and NP [see Fig. 2(a)–(c)]. The modulation index curves obtained along the ISW profile in each of the three polarized feature images are depicted in Fig. 2(d)–(f). The modulation index (δ) is calculated by extracting values along the red cross section and normalizing them based on the mean value in the white box.

Four large internal solitons are depicted in three polarized feature images, all of which effectively illustrate the scattering characteristics of ISWs. Comparatively, the maximum modulation index δ at internal soliton in the VV image is approximately 3.3, while the modulation index in the PD is approximately 3, which is comparable to the VV modulation. The NP image has the greatest modulation index variation, with a maximum of 8, which is more than double that of the VV image. NP contribution has a significant influence in the polarization scattering of ISWs. In addition, the results obtained for the L-band image in this example are consistent with those presented by da Silva et al. in a previous work, where the NP modulation found in the X-band is twice that of the VV modulation [27].

A. Polarization Scattering Intensity

Using the method described in Section II-B, a total of ten scenes of ALOS PALSAR images and ten scenes of ENVISAT

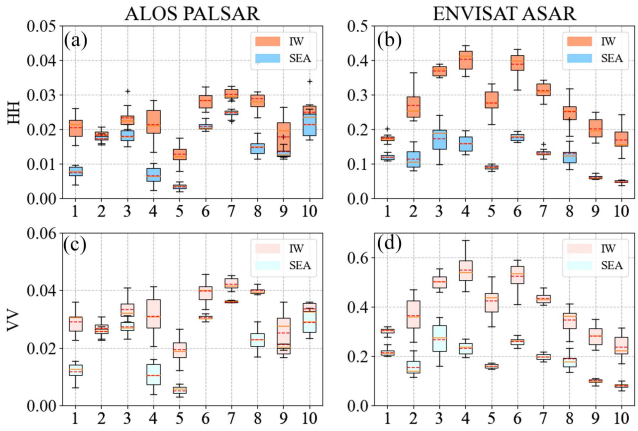

Fig. 3. Comparison of the polarization scattering intensity in ISW perturbation regions and sea surface regions, (linear units). (a), (b), (c), (d) shows the results of HH or VV polarization in L-band and C-band, respectively.

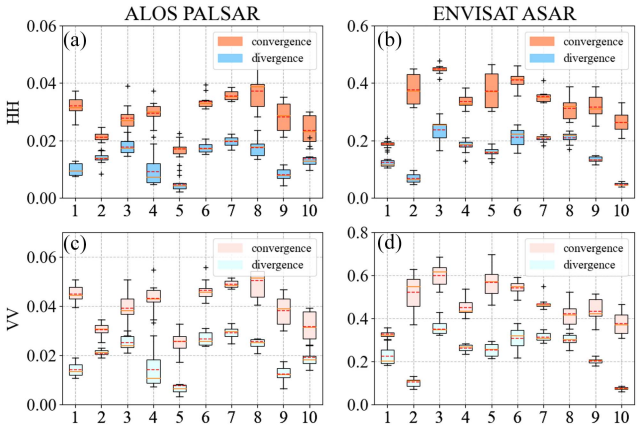

Fig. 4. Comparison of the polarization scattering intensity in ISW convergent zones and ISW divergent zones, (linear units). (a), (b), (c), (d) shows the results of HH or VV polarization in L-band and C-band, respectively.

ASAR images are processed to examine the polarization scattering characteristics of ISWs in detail.

First, the PD, NP, NP/HH, and NP/VV (representing the relative contribution of NP scattering concerning copolarized scattering) feature images were acquired. Second, ten subregions of interest were selected for each feature image, encompassing areas related to ISW, calm sea surfaces, as well as convergent and divergent zones. Finally, the mean values of all the data within each subregion were calculated and are graphically presented in box diagrams.

This section analyzes the scattering characteristics of ISWs in copolarized HH and VV images, which represent the scattering energy intensity. Fig. 3 depicts the polarized scattering intensity in the region perturbed by ISWs and the region of calm sea surface under HH and VV. Fig. 4 compares the polarized scattering intensity in the convergent and divergent zones of ISWs. On the left and right are the respective results for PALSAR(L) and ASAR(C).

The copolarized scattering intensity of ISW region is always greater than that of the undisturbed sea surface region in both two

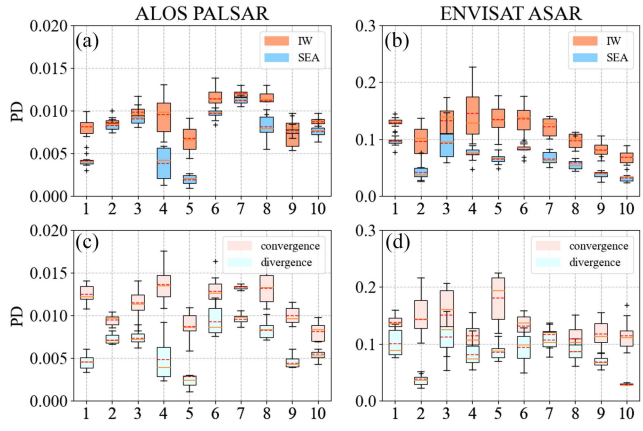

Fig. 5. Box plot of the PD representing the two-scale Bragg scattering characteristics. (a), (b) Results for the ISW perturbation regions and calm sea surface regions. (c), (d) Results of the convergent and divergent zones. The L-band is displayed on the left and the C-band on the right.

bands depicted in Fig. 3. In the L band, the scattering intensity of the ISW region in the HH(VV) image is approximately 52% (45%) greater than that of the sea surface region, while in the C band, it is 2.3(2.1) times that of the sea surface region. This suggests that there may be an additional scattering mechanism in ISW region, giving it much greater scattering energy than the surrounding sea surface. In contrast, Fig. 4 demonstrates that the polarized scattering intensity associated with the ISW convergent zone is always greater than the value associated with the divergent zone, which is capable of scattering back more electromagnetic waves in both HH and VV channels.

The above results indicate that the sea surface can scatter more electromagnetic waves in the region of ISW disturbance, particularly in the convergent zone, causing the SAR image to display more prominent characteristics. However, what is the reason for this phenomenon?

Alpers demonstrated in the literature that internal waves are related to the spatiotemporal variation of the surface currents, which interacts with the surface wind waves to modulate Bragg scattering [14]. Therefore, at low and intermediate incidence angles, the Bragg scattering mechanism is a potential explanation, and Fig. 2(e) shows a large PD modulation. In addition, Fig. 2(f) shows that the NP scattering variation in ISW perturbation region is also highly significant, which may also be an essential factor in the increased energy scattering in ISW perturbation region (convergent zone).

B. Copolarized Bragg Scattering: PD

To examine the effect of polarized Bragg scattering on the SAR detection of ISWs, the PD is considered in this section, and the effects of nonpolarized scattering (NP) have been removed from its computation. As seen from Fig. 5, the PD values in ISW perturbation regions are more than that of the calm sea surface regions, and the PD values in the convergent zones are bigger than that of the diverging zones, which is consistent with the total scattering intensity presented in Section III-A. In the L(C) band, the average PD value of the ISW perturbation region is

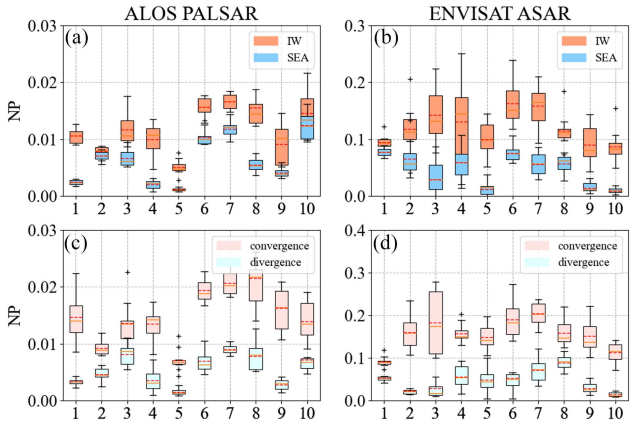

Fig. 6. Nonpolarized scattering features (NP), displayed in box plot. (a), (b) Results for the ISW perturbation region and the calm sea surface region. (c), (d) Results for the convergent and divergent zones. The L-band is shown on the left and the C-band on the right.

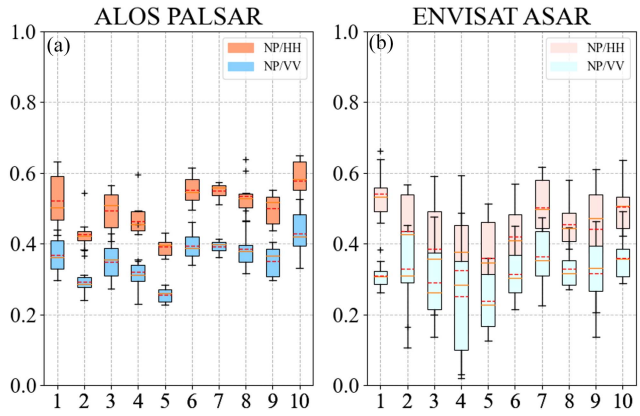

Fig. 7. Effect of nonpolarized scattering (NP) on HH and VV polarization in ISW perturbation region (NP/σ^0_{HH} and NP/σ^0_{VV}). The L-band is shown on the left (a) and the C-band on the right (b).

1.3(1.7) times that of the sea surface region, but the average PD value of the ISW convergent zones is approximately 75% (65%) greater than that of the divergent zones.

PD is governed by the surface roughness generated by the wave component close to the Bragg wave number, which contains the fast response change information about the short-scale Bragg waves. Based on the incidence angle and wavelength, the L-band resonant Bragg wavelength is between 30 and 40 cm, and that of the C-band is between 5 and 10 cm. The above results show that there is an enhanced decimeter-scale or centimeter-scale polarized Bragg scattering mechanism in ISW perturbation regions, especially in the convergent zone. This is related to breaking waves caused by ISWs. The continuous input of energy from ISWs modulated surface currents leads to additional energy dissipation (wave breaking), thereby enhancing the generation of short gravity waves that carrying shorter Bragg waves.

C. Nonpolarized Scattering: NP

Both in suit observations and optical images have found that there is a large distribution of whitecaps caused by breaking waves in ISWs perturbation regions. This is related to its resonance with the meter-scale surface waves, leading to breakup and crest overturning, which in turn produces considerable NP contributions [34], as illustrated by the NP modulation index in Fig. 2(e). This section examines the variation of NP in ISW perturbation region (sea surface area) and the convergent zone (divergent zone) in detail.

As depicted in Fig. 6, the NP value of the ISW perturbation region is always larger than that of the calm sea surface region. On average, in the L(C) band, the NP of ISW region is approximately 82% (165%) greater than that of the unperturbed sea surface region. Moreover, the NP contribution associated with the convergent zone is always larger than that associated with the diverging zone, approximately three times larger. This suggests that there is a stronger NP scattering contribution associated with the large number of waves breaking and near-wave breaking events in the convergent zone. ISWs will enhance the height of surface waves in the convergent zone. Resonance occurs when the group velocity of surface waves matches the phase speed of ISWs [35]. Powered by the continual input energy of ISWs, resonant surface waves continue to grow until they are dissipated or break up directly by transferring energy to shorter waves through nonlinear hydrodynamic interactions. In addition, the C band has a smaller scale (3.75–7cm), making it more sensitive to the response of breaking waves; hence, the NP in the ISW perturbation region under the C band is significantly greater than that in calm sea surface region.

Contributions of NP scattering related to copolarized HH and VV backscattering, NP/σ^0_{HH} and NP/σ^0_{VV}, are further analyzed. Fig. 7 demonstrates that the effect of NP scattering on HH is greater than its effect on VV in ISW perturbation region, whether in the L-band or C-band. Particularly, in the L-band, the average NP/σ^0_{HH} and NP/σ^0_{VV} are 0.52 and 0.36, respectively, while in the C-band, they are 0.43 and 0.31. The results suggest that the NP scattering mechanism has a significant impact on the total polarization scattering in ISW SAR scattering.

The effect of nonpolarized scattering (NP) on HH and VV polarization is also analyzed in ISW convergent zones and divergent zones, as shown in Fig. 8. In two bands, the effect of NP on HH is always greater than its effect on VV, both in the convergent zones and the divergent zones. In the convergent zones, the L(C) band, the average contribution of NP relative to the HH and VV is approximately 52% (37%) and 46% (33%), respectively, indicating that the contribution of NP in HH polarization is about 40% higher than that in the VV polarization. In contrast, in the divergent zones, the average values of NP/σ^0_{HH} and NP/σ^0_{VV} decreased to 42% (28%) and 29% (19%), respectively. These results corroborate the significant NP contribution associated with ISW convergent zones.

The above results suggest that the NP scattering has a significant effect on ISW SAR backscattering. In overall ISW perturbation regions, whether the convergent or divergent zones, the effect of NP on HH is greater than its effect on VV. This is determined by the NP scattering properties of the breaking waves. The NP scattering is independent of polarization, and

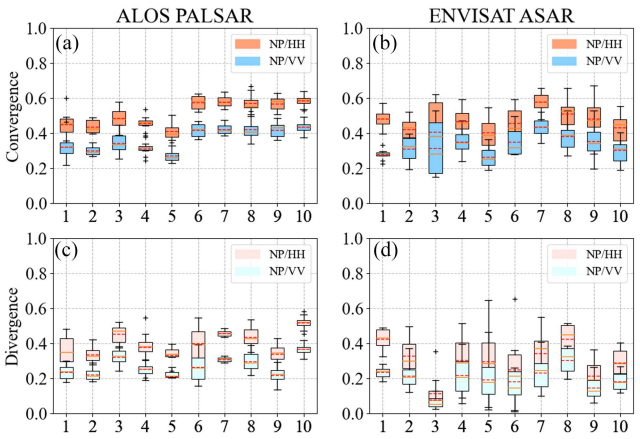

Fig. 8. Contribution of nonpolarized scattering (NP) with respect to the HH and VV polarization. (a), (c) Convergent zone. (b), (d) Divergent zone.

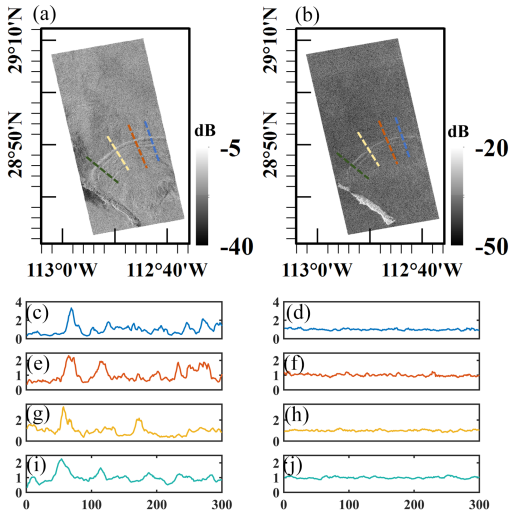

Fig. 9. Polarization features of ALOS PALSAR images, acquired on November 3, 2009, with an incidence angle is 25.75°. (a) HH. (b) HV. (c), (d), (e), (f), (g), (h), (i), (j) Modulation index, indicted based on the profile of interest. The subpanels (c/e/g/i) correspond to the colored solid lines in (a), while the subpanels (d/f/h/j) correspond to (b).

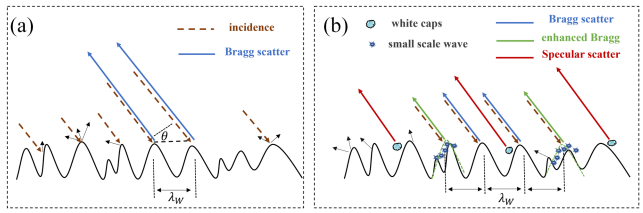

Fig. 10. Structure of the SAR scattering echo after ISWs modulate the surface. (a) Bragg scattering θ is the incident angle, and λ_W is the resonant wavelength. (b) Presence of additional short-scale waves and breaking waves enhances the Bragg scattering and the specular scattering.

the Bragg scattering contribution under the VV polarization at intermediate incident angles (20°∼30°) is greater than that in HH, while the HH NRCS is lower than VV NRCS on average, resulting in a greater contribution of nonpolarized scattering in HH [36]. Note that we are concerned with the effect of NP scattering on polarization scattering and do not intend to make a direct comparison regarding whether the effect of NP scattering on the L-band is greater than that on the C-band. As seen in Figs. 7 and 8, a larger variation in NP contribution among the entire SAR dataset can be seen, which may be related to different sea conditions and sensor parameters during SAR data acquisition.

D. Cross-Polarization Scattering

NP backscattering can come from both specular scattering and incoherent scattering due to small-scale surface roughness disturbances caused by breaking waves. In the latter case, strong first-order resonant polarized small-scale scattering cannot occur, the nonpolarized and cross-polarized contributions dominate [37]. Section III-B has proved that ISWs enhance the polarized Bragg scattering, and this section focuses on analyzing whether ISWs have significant cross-polarization features.

Fig. 9 illustrates a set of ISW packet features acquired on the west coast of the United States, with multiple solitons propagating to the southwest. Fig. 9(a) is the HH polarization and Fig. 9(b) depicts the cross-polarization polarization (HV). Compared with HH, the scattering energy in HV is weak, although the leading wave can be clearly displayed, many detailed features cannot be described. Four profiles of interest are selected in the image along the propagation direction of ISWs, and the corresponding modulation index curves are obtained. The modulation index curves reveal that ISWs in HH are characterized by multiple solitons, whereas they are almost impossible to distinguish in HV. This suggests that the sea surface changes induced by ISWs are less sensitive to HV compared to copolarized HH and VV, and hence, the characterization of NP scattering in HV is not performed in this article. This not only excludes the second potential source of NP scattering, but also implies that the depolarization of ISWs is weak.

We suggest that the strong nonpolarized scattering (NP) caused by ISWs is mainly due to the enhanced specular reflection after the modulation of the sea surface. SAR mainly observes calm seas through the Bragg scattering mechanism at intermediate incidence angles during side-looking observations. When ISWs modulate the roughness of the sea surface and induce surface wave breaking, short-scale waves and other rough structures are generated. This not only enhances Bragg scattering, but also enhances the specular reflection in the SAR side-looking observation structure. As depicted in the Fig. 10, it may originate from quasi-specular reflection of themodulated regular surface (not broken), or it originates from specular scattering provided by breaking waves. Section IV further discusses this based on the polarization decomposition feature parameters.

IV. Discussion

A. Polarimetric Scattering Mechanism

The existence of ISWs significantly alters the SAR scattering properties at the sea surface, such as NP scattering theory indicates that the breaking waves pay a pivotal role in the SAR NRCS

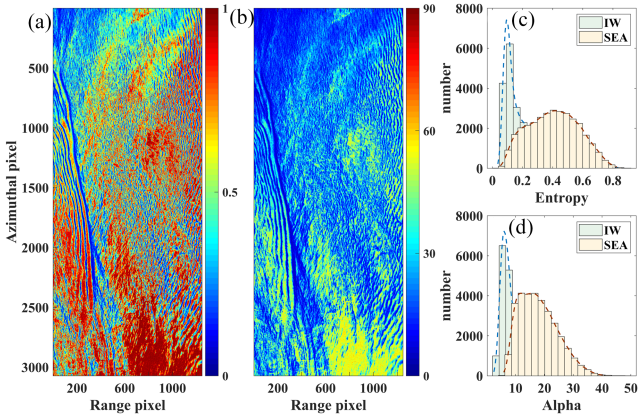

Fig. 11. Polarization features obtained by processing of ALOS PALSAR image, acquired in Andaman Sea on April 14, 2007. (a) Polarization entropy (H). (b) Average scattering angle (α). (c) H probability density distribution, (d) α probability density distribution.

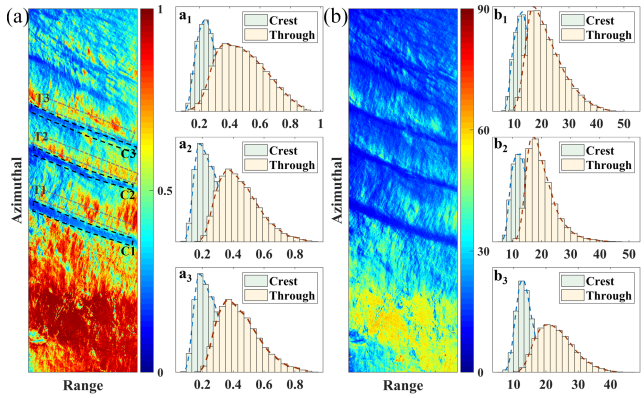

Fig. 12. Polarization features obtained by processing of ALOS PALSAR image acquired in Sulu Sea on May 19, 2010. (a) Polarization entropy (H). (b) Average scattering angle (α). a1-a3 (b1-b3) are the results of convergence and divergence of the three solitons, respectively.

of ISW through mechanisms like Bragg scattering and specular scattering. In this section, further discussion is carried out based on the polarization decomposition theory to demonstrate the polarization scattering properties of ISWs.

Fully polarized SAR provides a wealth of polarization feature parameters by polarization decomposition, which can effectively characterize the primary scattering characteristics of the detected target [38], [39]. In the case of the ALOS PALSAR images used earlier, which are fully polarized, we employed the H$A\alpha$ decomposition to extract key parameters such as the average scattering angle (α) and the polarization entropy (H) [40], as shown in Fig. 11. The H describes the randomness of the target scattering, and its value ranges from 0 to 1, the larger the value, the higher the scattering randomness. The α is between [0–90°], which reflects the scattering mechanism of the detection target, and with the increase of α, the target scattering mechanism gradually changes from surface scattering to volume scattering. The analysis of the polarization feature images in Fig. 11 reveals that, compared with the calm sea surface, the H value of ISW perturbation region is mainly between 0.1–0.3, which is significantly lower than the that of 0.2–0.6 in the surrounding sea surface, implying that the scattering randomness of ISW is lower, and more electromagnetic waves can be returned to the sensor.

In the α image, the value range of ISW perturbation region is mainly between 5° and 15°, which is much lower than that of 10° to 40° in the surrounding sea surface. After ISWs cause the surface waves to break, the scattering angle becomes smaller, which not only shows that the scattering mechanism is closer to surface scattering, but also strengthens the contribution of nonpolarized scattering (NP). This is consistent with the analysis results in Section III-C. The main reason is that ISWs modulate the sea surface regularly and dramatically, forming rough strips and breaking waves, and producing a geometric structure similar with the specular scattering under SAR side-looking observation (see Fig. 9).

Fig. 12 depicts the results of $HA\alpha$ decomposition of another PALSAR image to further investivate the scattering mechanism of ISW convergent zones and divergent zones. There are four internal solitons propagating in the azimuthal direction, and the convergent and divergent zones of the first third solitons are extracted for analysis, as shown in the blue and gray boxes, respectively. Fig. 12(a) is the result of the processing of H, which gives the probability density distribution of the three solitons (convergent zones and divergent zones, respectively). The results indicate that the H values in ISW convergent zones are all less than that in the divergent zones, that is, scattering randomness of the convergence is weaker. The results of α show that the scattering angles of the convergent zones are much smaller than that of the divergent zones, indicating that the convergent zone is closer to specular scattering. This is consistent with the above analysis that ISWs modulate the sea surface, which not only enhances the Bragg scattering but also the specular scattering. This enhanced specular scattering may come from either the breaking waves or the quasi-specular reflection from a regular surface (unbroken) after modulation by an ISW.

Compared with the calm sea surface, the polarization entropy and average scattering angle of ISW perturbation regions are lower, and these two polarization feature parameters can characterize the depolarization ability. When the scattering mechanism is more complex and volume scattering predominates, the depolarization capability is greater [41]. Changes induced by ISWs at the sea surface alter their scattering mechanism and reduce the scattering randomness. The presence of breaking waves causes specular scattering, implying a weaker depolarization ability of ISWs.

We further process the original ALOS PALSAR images to obtain polarization feature parameters, such as the degree of polarization (DoP), which can directly characterize the depolarization ability [42]. DoP includes the degree of linear polarization (DoLP) and the degree of circular polarization (DoCP). They are expressed as follows, when they are equal to 1, representing complete polarization

$$DoLP = \frac{\sqrt{g_2^2 + g_3^2 + g_4^2}}{g_1}, DoCP = \frac{g_3}{g_1} \tag{6}$$

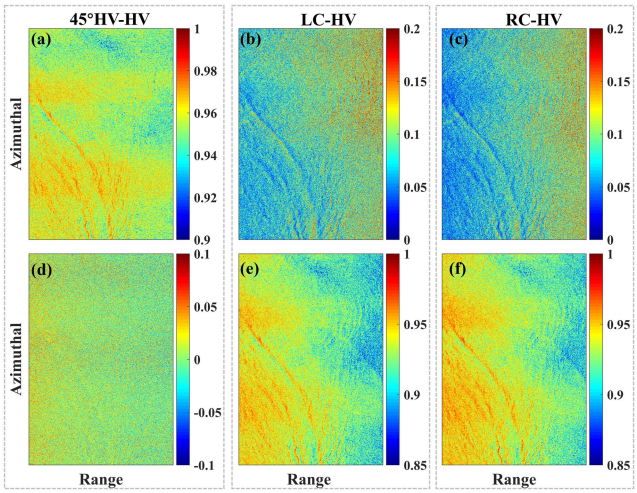

Fig. 13. DoLP and the degree of circular polarization (CoLP) obtained by reconstructing the compact polarized data based on ALOS PALSAR. (a) and (d) DoLP and CoLP in linear copolarization compact polarization (45° HV-HV), respectively. (b) and (e) DoLP and CoLP in hybrid left circular compact polarization (LC-HV), respectively. (c) and (f) DoLP and CoLP in hybrid right circular compact polarization (RC-HV), respectively.

$g_{j,j=1\sim4}$ is the Stokes vector in the compact polarization mode. The compact polarization is a special type of dual-polarized SAR that transmits only linearly polarized or circularly polarized waves in one direction, but simultaneously receives horizontal and vertical echoes or circularly polarized echoes [43]. Several compact polarized SAR images can be obtained depending on the polarization mode of the electromagnetic waves and the direction of the incident angle.

At present, there is a lack of actual compact polarized SAR images. After processing the original fully polarized PALSAR images, the compact polarized images are reconstructed using different polarization modes and electromagnetic wave directions. In the reconstruction process, the receiving electromagnetic wave is fixed as linear polarization R_x = (H, V), whereas the transmitting wave is set as 45° linear polarization (T_x = 45°HV), left circular polarization (T_x = LC), and right circular polarization (T_x = RC). The obtained compact polarized images include linear co-polarization (45° HV-HV) and hybrid polarization (LC-HV, RC-HV), finally, the corresponding polarization degree is further extracted.

DoLP and DoCP are calculated for each of the three compact polarized SAR images depicted in Fig. 13, which were generated using PALSAR images. As shown, the DoLP and DoCP obtained by the same compact polarized mode exhibit opposite characteristics. In Fig. 13(a), the DoLP at ISW perturbation region is larger, while in the corresponding DoCP (13d) the ISW almost disappear, because the mode does not contain circular polarization information. In the hybrid compact polarized mode, ISWs are very significant in the corresponding DoCP (13e/f), and its value is close to 1; while the intensity of DoCP (13b/c) is weak.

These results demonstrate that the DoP of ISW perturbation regions is significantly greater than that of the surrounding calm sea surface, confirming its stronger polarization capability.

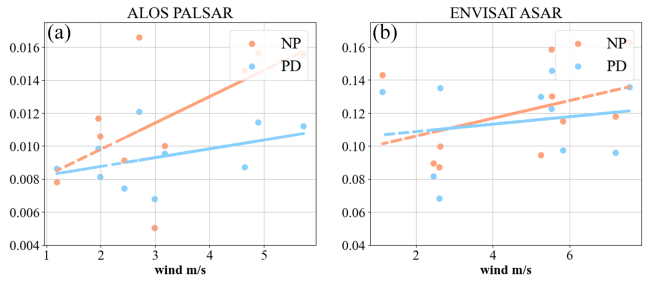

Fig. 14. Relationship between the average NP scattering and average PD scattering and wind speed at ISWs. (a) 10 L-band images. (b) 10 C-band images.

The literature [44] shows that the copolarization features are more significant and the degree of polarization is greater when the specular scattering is stronger. This is consistent with the analytical results above, since the ISW-induced breaking waves enhance the specular scattering. In addition, compared with the linear compact polarization data, the response performance of ISWs is improved by using the hybrid compact polarization, which can provide more information.

B. *Impact of Environment*

The surface breaking waves induced by ISWs undergoes significant variations due to various factors, such as wind speed, wind direction, topography, the speed and amplitude of ISWs, and more. The background wind field can input energy into surface waves, thus influencing the extent of wave breaking. Previous research has indicated that radar backscatter from breaking waves is highest in upwind conditions and lowest in downwind conditions [45]. Fig. 14 illustrates the variations in average NP scattering and average PD scattering at ISW in the L (C) band with changes in wind speed. The distribution of data points in the figure is quite heterogeneous. While the fitted lines in the figure exhibit a positive correlation, further experimentation is considered necessary in this study to quantitatively analyze the correlation between the polarization scattering characteristics of breaking waves and the wind field at the sea surface.

In addition to the wind field, changes in topography, specifically variations in water depth, can also significantly impact the process of ISWs inducing wave breaking. ISWs undergo pronounced changes in topography during their propagation. For instance, in the northern South China Sea, ISWs originate in the Luzon Strait and travel westward for several hours before dissipating. Along this journey, they traverse deep-sea basins, continental slopes, and nearshore continental shelves, encountering water depth variations exceeding 3000 m. The two-layer fluid theories that describe the motion of ISWs, such as the KdV, eKdV, and MCC equations, suggest that changes in water depth led to variations in nonlinear and dispersion coefficients, thereby affecting the wavelength, amplitude, and phase speed of ISWs [46]. Consequently, due to the influence of topographical changes, the characteristics of ISWs undergo significant alterations, impacting their interaction with surface waves and directly modulating wave breaking.

On one hand, ISWs with different amplitudes can generate surface waves with varying amplitudes at the sea surface [47]. This leads to the convergence of water particles, steepening of waves, and an increased probability of wave breaking. On the other hand, the speed of ISWs is closely linked to the breaking of surface waves. When the group velocity of surface waves is close to the phase velocity of ISWs, resonance occurs, causing energy accumulation and eventual overturning and breaking of wave crests. Please note that we primarily focus on the impact of breaking waves induced by ISWs on SAR scattering. Further comparison and analysis of the differences in breaking waves generated under different background environments are beyond the scope of this article.

V. Conclusion

After ISWs resonate with the meter-level surface waves, the modulated sea surface exhibits a significant roughness variation and wave breaking. The scattering mechanism associated with breaking waves caused by ISWs is investigated. Polarized Bragg scattering contribution (PD) and nonpolarized scattering contribution (NP) associated with breaking waves are obtained from the copolarized SAR images based on the nonpolarized scattering theory.

The scattering intensity in ISW perturbation regions is greater than that of the surrounding sea surface, with enhanced SAR response characteristics, such as enhanced polarized Bragg scattering and additional nonpolarized scattering. The interaction of the changing currents induced by ISWs with the sea surface wind waves modifies the roughness (i.e., mean square slope), and the surface waves gradually break up, generating additional short-scale waves and many bubbles, which contribute to SAR echo through Bragg scattering and specular scattering.

First, the short-scale waves carrying Bragg waves enhance the decimeter or centimeter-scale polarized Bragg scattering, particularly in the convergent zones. The estimated polarization Bragg scattering contribution (PD) of the convergent zones is about 65%–75% higher than that of the divergent zones. The results of polarization decomposition also show that the degree of polarization of ISW increases and the scattering entropy decreases.

Second, the breaking waves enhance the specular scattering probability under the SAR side-looking detection structure, which not only facilitates the copolarized scattering, but also enables the ISW perturbation regions to obtain additional nonpolarized scattering contribution. The modulation of ISWs in the nonpolarized scattering contribution is about 3–5 times higher than that in the polarized scattering contribution. The nonpolarized scattering associated with the convergent zones is larger than that associated with the divergent zones, and both its effects on the HH are greater than that on the VV. The results of polarization decomposition indicate that the average scattering angle and the scattering randomness are greatly reduced at ISW perturbation regions, especially in convergent zones, further supporting the inference that enhanced specular scattering.

This article highlights the SAR echo contribution of surface breaking waves caused by ISWs. The focus of future work is to comprehensively analyze the SAR scattering characteristics of ISWs under different wind conditions, topography, wave bands, incident angles, and degree of breaking waves through modeling, which requires many assumptions and experiments.

Acknowledgment

The authors would like to thank the European Space Agency (ESA) for providing ENVISAT ASAR images, the Japan Aerospace Exploration Agency (JAXA) for providing the ALOS PALSAR images.

Appendix

ALOS PALSAR and Envisat ASAR imagery information used for computational analysis.

SAR image id	date	incidence /°	wind m/s
ALPSRP065000100-L1.1	20070414	23.974	1.984
ALPSRP071350010-L1.1	20070528	23.95	1.19
ALPSRP079032420-L1.1	20070719	23.921	1.954
ALPSRP167617030-L1.1	20090318	24.085	3.169
ALPSRP167617040-L1.1	20090318	23.964	2.983
ALPSRP171847130-L1.1	20090416	23.978	4.892
ALPSRP193880020-L1.1	20090914	23.962	2.707
ALPSRP201180570-L1.1	20091103	25.745	5.726
ALPSRP274397160-L1.1	20110320	23.945	2.433
ALPSRP275546710-L1.1	20110328	24.182	4.646
ASA_APP_1PNESA20070531	20070531	33.64	5.245
ASA_APP_1PNESA20070630	20070630	21.299	7.19
ASA_APP_1PNESA20070716	20070716	22.241	1.1317
ASA_APP_1PNESA20070903	20070903	22.281	5.529
ASA_APP_1PNESA20070915	20070915	22.324	2.625
ASA_APP_1PNESA20071213	20071213	22.33	7.546
ASA_APP_1PNESA20071217	20071217	22.316	5.526
ASA_APP_1PNESA20080410	20080410	22.271	5.828
ASA_APP_1PNESA20080420	20080420	22.246	2.451
ASA_APP_1PNESA20080420	20080420	22.249	2.599

References

[1] T. Gerkema and J. Zimmerman, "An introduction to internal waves," Lecture Notes, Royal NIOZ, Texel, pp. 16–18, 2008.

[2] K. R. Helfrich and W. K. Melville, "Long nonlinear internal waves," *Annu. Rev. Fluid Mech.*, vol. 38, pp. 395–425, 2006, doi: 10.1146/annurev.fluid.38.050304.092129.

[3] C. R. Jackson, J. C. B. da Silva, and G. Jeans, "The generation of nonlinear internal waves," *Oceanography*, vol. 25, no. 2, pp. 108–123, 2012, doi: 10.5670/oceanog.2012.46.

[4] Y.-H. Wang, C.-F. Dai, and Y.-Y. Chen, "Physical and ecological processes of internal waves on an isolated reef ecosystem in the South China Sea," *Geophysical Res. Lett.*, vol. 34, no. 18, pp. 609–615, 2007, doi: 10.1029/2007GL030658.

[5] Y. Liu et al., "Late monsoon threatens coral refugia in the Andaman Sea," *Environ. Res. Lett.*, vol. 17, 2022, Art. no. 034038.

[6] V. Bondur, A. Serebryany, and V. Zamshin, "Registering fish shoals attracted by solitary intensive internal waves," *Doklady Earth Sci.*, vol. 492, pp. 471–474, 2020, doi: 10.1134/S1028334X20060033.

[7] S. E. Moore and R.-C. Lien, "Pilot whales follow internal solitary waves in the South China Sea," *Mar. Mammal Sci.*, vol. 23, no. 1, pp. 193–196, 2007, doi: 10.1111/j.1748-7692.2006.00086.x.

[8] J. Pineda, S. Rouse, V. Starczak, K. Helfrich, and D. Wiley, "Response of small sharks to nonlinear internal waves," *Limnol. Oceanogr.*, vol. 65, no. 4, pp. 707–716, 2020, doi: 10.1002/lno.11341.

[9] Y. Gong, J. Xie, J. Xu, Z. Chen, Y. He, and S. Cai, "Oceanic internal solitary waves at the Indonesian submarine wreckage site," *Acta Oceanologica Sinica*, vol. 41, pp. 109–113, 2021, doi: 10.1007/s13131-021-1893-0.

[10] C. R. Jackson, J. C. B. da Silva, G. Jeans, W. Alpers, and M. J. Caruso, "Nonlinear internal waves in synthetic aperture radar imagery," *Oceanography*, vol. 26, no. 2, pp. 68–79, 2013, doi: 10.5670/oceanog.2013.32.

[11] J. Bole, C. Ebbesmeyer, and R. Romea, "Soliton currents in the South China Sea: Measurements and theoretical modeling," in *Proc. Offshore Technol. Conf.*, 1994, pp. 367–376, doi: 10.4043/7417-MS.

[12] V. Klemas, "Remote sensing of ocean internal waves: An overview," *J. Coastal Res.*, vol. 28, no. 3, pp. 540–546, 2012, doi: 10.2112/JCOAS-TRES-D-11-00156.1.

[13] A. Moreira, P. Prats-Iraola, M. Younis, G. Krieger, I. Hajnsek, and K. P. Papathanassiou, "A tutorial on synthetic aperture radar," *IEEE Geosci. Remote Sens. Mag.*, vol. 1, no. 1, pp. 6–43, Mar. 2013, doi: 10.1109/MGRS.2013.2248301.

[14] W. Alpers, "Theory of radar imaging of internal waves," *Nature*, vol. 314, no. 6008, pp. 245–247, 1985, doi: 10.1038/314245a0.

[15] S. Bao, J. Meng, L. Sun, and Y. Liu, "Detection of ocean internal waves based on faster R-CNN in SAR images," *J. Oceanol. Limnol.*, vol. 38, no. 1, pp. 55–63, 2020, doi: 10.1007/s00343-019-9028-6.

[16] S. Celona et al., "Automated detection, classification, and tracking of internal wave signatures using X-band radar in the inner shelf," *J. Atmospheric Ocean. Technol.*, vol. 38, no. 4, pp. 789–803, 2021, doi: 10.1175/JTECH-D-20-0129.1.

[17] C. Guo, V. Vlasenko, W. Alpers, N. Stashchuk, and X. Chen, "Evidence of short internal waves trailing strong internal solitary waves in the northern South China Sea from synthetic aperture radar observations," *Remote Sens. Environ.*, vol. 124, pp. 542–550, Dec. 2012, doi: 10.1016/j.rse.2012.06.001.

[18] T. Jia, J. Liang, Q. Li, J. Sha, and X.-M. Li, "Generation of shoreward nonlinear internal waves south of the Hainan Island: Synthetic aperture radar observations and numerical simulations," *J. Geophysical Res., Oceans*, vol. 126, no. 6, pp. 17334–17349, Jun. 2021, doi: 10.1029/2021JC017334.

[19] I. Kozlov, V. Kudryavtsev, E. Zubkova, A. Zimin, and B. Chapron, "Characteristics of short-period internal waves in the Kara Sea inferred from satellite SAR data," *Izvestiya, Atmospheric Ocean. Phys.*, vol. 51, no. 9, pp. 1073–1087, 2015, doi: 10.1134/S0001433815090121.

[20] A. A. Kurekin, P. E. Land, and P. I. Miller, "Internal waves at the U.K. continental shelf: Automatic mapping using the ENVISAT ASAR sensor," *Remote Sens.*, vol. 12, no. 15, pp. 2476–2496, 2020, doi: 10.3390/rs12152476.

[21] X. Li, P. Clemente-Colón, and K. S. Friedman, "Estimating oceanic mixed-layer depth from internal wave evolution observed from Radarsat-1 SAR," *Johns Hopkins APL Tech. Dig.*, vol. 21, no. 1, pp. 130–135, 2000.

[22] C. R. de Macedo, J. C. B. da Silva, A. Buono, and M. Migliaccio, "Multi-polarization radar backscatter signatures of internal waves at L-band," *Int. J. Remote Sens.*, vol. 43, no. 6, pp. 1943–1959, 2022, doi: 10.1080/01431161.2022.2050435.

[23] J. M. Magalhães and J. C. B. da Silva, "Internal solitary waves in the Andaman Sea: New insights from SAR imagery," *Remote Sens.*, vol. 10, no. 6, pp. 861–876, 2018, doi: 10.3390/rs10060861.

[24] H. Zhang, J. Meng, L. Sun, X. Zhang, and S. Shu, "Performance analysis of internal solitary wave detection and identification based on compact polarimetric SAR," *IEEE Access*, vol. 8, pp. 172839–172847, 2020, doi: 10.1109/ACCESS.2020.3025946.

[25] W. K. Melville, "The role of surface-wave breaking in air-sea interaction," *Annu. Rev. Fluid Mechanics*, vol. 28, no. 1, pp. 279–321, 1996, doi: 10.1146/annurev.fl.28.010196.001431.

[26] J. M. Santos-Ferreira et al., "Effects of surface wave breaking caused by internal solitary waves in SAR altimeter: Sentinel-3 Copernicus products and advanced new products," *Remote Sens.*, vol. 14, no. 3, 2022, Art. no. 587, doi: 10.3390/rs14030587.

[27] J. M. Magalhães, W. Alpers, A. M. Santos-Ferreira, and J. C. B. da Silva, "Surface wave breaking caused by internal solitary waves effects on radar backscattering measured by SAR and radar altimeter," *Oceanography*, vol. 34, no. 2, pp. 166–176, 2021, doi: 10.5670/oceanog.2021.203.

[28] V. N. Kudryavtsev, B. Chapron, A. G. Myasoedov, F. Collard, and J. A. Johannessen, "On dual co-polarized SAR measurements of the ocean surface," *IEEE Geosci. Remote Sens. Lett.*, vol. 10, no. 4, pp. 761–765, Jul. 2013, doi: 10.1109/LGRS.2012.2222341.

[29] V. N. Kudryavtsev, S. Fan, B. Zhang, A. A. Mouche, and B. Chapron, "On quad-polarized SAR measurements of the ocean surface," *IEEE Trans. Geosci. Remote Sens.*, vol. 57, no. 11, pp. 8362–8370, Nov. 2019, doi: 10.1109/TGRS.2019.2920750.

[30] I. A. Sergievskaya et al., "Modulation of dual-polarized X-band radar backscatter due to long wind waves," *Remote Sens.*, vol. 11, no. 4, pp. 423–438, 2019, doi: 10.3390/rs11040423.

[31] H. Hersbach et al., "The ERA5 global reanalysis," *Quart. J. Roy. Meteorol. Soc.*, vol. 146, no. 730, pp. 1999–2049, 2020, doi: 10.1002/qj.3803.

[32] H. Hersbach et al., "ERA5 hourly data on single levels from 1979 to present," Copernicus Climate Change Service (C3S) Climate Data Store (CDS), 2018, doi: 10.24381/cds.adbb2d47. [Online]. Available: https://cds.climate.copernicus.eu/cdsapp#!/dataset/reanalysis-era5-single-levels?tab=overview

[33] V. Kudryavtsev, D. Akimov, J. Johannessen, and B. Chapron, "On radar imaging of current features: 1. Model and comparison with observations," *J. Geophysical Res., Oceans*, vol. 110, no. C7, pp. C07016 1–27, 2005, doi: 10.1029/2004JC002505.

[34] S. A. Ermakov, I. A. Sergievskaya, and I. A. Kapustin, "Strong modulation of short wind waves and ka-band radar return due to internal waves in the presence of surface films. Theory and experiment," *Remote Sens.*, vol. 13, no. 13, 2021, Art. no. 2462, doi: 10.3390/rs13132462.

[35] W. Craig, P. Guyennev, and C. Sulem, "The surface signature of internal waves," *J. Fluid Mechanics*, vol. 7, no. 10, pp. 277–303, 2012, doi: 10.1017/jfm.2012.364.

[36] J. A. Johannessen, V. Kudryavtsev, D. Akimov, T. Eldevik, N. Winther, and B. Chapron, "On radar imaging of current features: 2. Mesoscale eddy and current front detection," *J. Geophysical Res., Oceans*, vol. 110, no. C7, pp. C07017 1–14, 2005, doi: 10.1029/2004JC002802.

[37] V. Kudryavtsev, S. Fan, B. Zhang, A. A. Mouche, and B. Chapron, "On quad-polarized SAR measurements of the ocean surface," *IEEE Trans. Geosci. Remote Sens.*, vol. 57, no. 11, pp. 8362–8370, Nov. 2019, doi: 10.1109/TGRS.2019.2920750.

[38] H. A. Zebker and J. J. Van Zyl, "Imaging radar polarimetry: A review," *Proc. IEEE*, vol. 79, no. 11, pp. 1583–1606, Nov. 1991, doi: 10.1109/5.118982.

[39] S. R. Cloude and E. Pottier, "A review of target decomposition theorems in radar polarimetry," *IEEE Trans. Geosci. Remote Sens.*, vol. 34, no. 2, pp. 498–518, Mar. 1996, doi: 10.1109/36.485127.

[40] S. R. Cloude and E. Pottier, "An entropy based classification scheme for land applications of polarimetric SAR," *IEEE Trans. Geosci. Remote Sens.*, vol. 35, no. 1, pp. 68–78, Jan. 1997, doi: 10.1109/36.551935.

[41] B.-H. Choe, D. Kim, J.-H. Hwang, Y. Oh, and W. M. Moon, "Detection of oyster habitat in tidal flats using multi-frequency polarimetric SAR data," *Estuarine, Coastal Shelf Sci.*, vol. 9, no. 7, pp. 28–37, 2012, doi: 10.1016/j.ecss.2011.11.007.

[42] R. Shirvany, M. Chabert, and J.-Y. Tourneret, "Ship and oil-spill detection using the degree of polarization in linear and hybrid/compact dual-pol SAR," *IEEE J. Sel. Topics Appl. Earth Observ. Remote Sens.*, vol. 5, no. 3, pp. 885–892, Jun. 2012, doi: 10.1109/JSTARS.2012.2182760.

[43] J.-C. Souyris and S. Mingot, "Polarimetry based on one transmitting and two receiving polarizations: The pi/4 mode," in *Proc. IEEE Int. Geosci. Remote Sens. Symp.*, 2002, vol. 1, pp. 629–631, doi: 10.1109/IGARSS.2002.1025127.

[44] J.-S. Lee, R. W. Jansen, D. L. Schuler, T. L. Ainsworth, G. O. Marmorino, and S. R. Chubb, "Polarimetric analysis and modeling of multifrequency SAR signatures from Gulf Stream fronts," *IEEE J. Ocean. Eng.*, vol. 23, no. 4, pp. 322–333, Oct. 1998, doi: 10.1109/48.725228.

[45] V. Kudryavtsev, D. Hauser, G. Caudal, and B. Chapron, "A semiempirical model of the normalized radar cross-section of the sea surface 1. Background model," *J. Geophysical Res., Oceans*, vol. 108, no. C3, pp. FET 2-1–FET 2-24, 2003, doi: 10.1029/2001JC001003.

[46] H. Du, G. Wei, S. D. Wang, and X. L. Wang, "Experimental study of elevation-and depression-type internal solitary waves generated by gravity collapse," *Phys. Fluids*, vol. 31, no. 10, 2019, Art. no. 102104, doi: 10.1063/1.5121556.

[47] M. Zhang, J. Wang, Z. Li, K. Liang, and X. Chen, "Laboratory study of the impact of the surface solitary waves created by the internal solitary waves on optical imaging," *J. Geophysical Res., Oceans*, vol. 127, no. 2, 2021, Art. no. e2021JC017800, doi: 10.1029/2021JC017800.

Hao Zhang (Student Member, IEEE) was born in Weifang, Shandong, China, in 1995. He received the M.S. degree in internal wave SAR detection from the First Institute of Oceanography, Ministry of Natural Resources of China, Qingdao, China, in 2021.

Since 2021, he has been working toward the Ph.D. degree with the China University of Petroleum, Qingdao, China. His research interests include internal wave remote sensing detection and internal wave altimeter analysis.

Junmin Meng (Member, IEEE) received the B.S. degree in mathematics and the M.S. degree in applied mathematics from Inner Mongolia Normal University, Urumqi, China, in 1996 and 1999, respectively, and the Ph.D. degree in physical oceanography from Ocean University of China, Qingdao, China, in 2002.

He is a currently a Professor with the First Institute of Oceanography, Ministry of Natural Resources, Qingdao, China. His research interests include ocean internal waves study with remote sensing data, SAR oceanic application, and ship detection with space and airborne radar.

Lina Sun was born in Huadian, Jilin, China, in 1985. She received the M.S. degree in optical physics from Ocean University of China, Qingdao, China in 2012.

Since 2012, she has been an Assistant Engineer with the First Institute of Oceanography, Ministry of Natural Resources, Qingdao, where she was an Engineer in 2018. Her research interests include the detection of ocean internal waves using remote sensing images and remote sensing data processing.

Shibao Li was born in 1978. He received the B.S. and M.S. degrees in computer science from the University of Petroleum, Beijing, China, in 2002 and 2009, respectively.

He is currently a Professor with the China University of Petroleum, Qingdao, China. His research interests include indoor localization technology, the Internet of Things, wireless networks, and mobile computing.

Xinmiao Zhang was born in 1999. Since 2021, she has been working toward the M.S. degree in oceanic internal waves through remote sensing images and numerical simulations with the First Institute of Oceanography, Ministry of Natural Resources of China, Qingdao, China.